ADVANCED FUNCTIONAL MATERIALS
www.afm-journal.de

Ferroelectric $Sr_3Zr_2O_7$: Competition between Hybrid Improper Ferroelectric and Antiferroelectric Mechanisms

Suguru Yoshida, Koji Fujita, Hirofumi Akamatsu, Olivier Hernandez, Arnab Sen Gupta, Forrest G. Brown, Haricharan Padmanabhan, Alexandra S. Gibbs, Toshihiro Kuge, Ryosuke Tsuji, Shunsuke Murai, James M. Rondinelli, Venkatraman Gopalan, and Katsuhisa Tanaka*

In contrast to polar cation displacements driving oxides into noncentrosymmetric and ferroelectric states, inversion-preserving anion displacements, such as rotations or tilts of oxygen octahedra about cation coordination centers, are exceedingly common. More than one nonpolar rotational mode in layered perovskites can lift inversion symmetry and combine to induce an electric polarization through a hybrid improper ferroelectric (HIF) mechanism. This form of ferroelectricity expands the compositional palette to new ferroelectric oxides because its activity derives from geometric rather than electronic origins. Here, the new Ruddlesden–Popper HIF $Sr_3Zr_2O_7$, which is the first ternary lead-free zirconate ferroelectric, is reported and room-temperature polarization switching is demonstrated. This compound undergoes a first-order ferroelectric-to-paraelectric transition, involving an unusual change in the "sense" of octahedral rotation while the octahedral tilt remains unchanged. Our experimental and first-principles study shows that the paraelectric polymorph competes with the polar phase and emerges from a trilinear coupling of rotation and tilt modes interacting with an antipolar mode. This form of hybrid improper "antiferroelectricity" is recently predicted theoretically but has remained undetected. This work establishes the importance of understanding anharmonic interactions among lattice degrees of freedom, which is important for the discovery of new ferroelectrics and likely to influence the design of next-generation thermoelectrics.

1. Introduction

For more than 60 years, ferroelectric ABO_3 perovskites and related compounds have been intensely studied, because they display technologically important ferroelectric hysteresis behavior for nonvolatile memory and large piezoelectric responses for actuators and sensors.[1–3] The most studied oxides are proper ferroelectrics such as $BaTiO_3$, $PbTiO_3$, and $BiFeO_3$, where the paraelectric-to-ferroelectric phase transition involves a zone-center polar lattice instability, typically driven by off-centering of closed-shell $3d^0$ Ti^{4+} ions and/or $6s^2$ stereochemically active lone-pair (SCALP) cations (Pb^{2+} and Bi^{3+}) via the so-called second-order Jahn–Teller effect (SOJT).[4–6] In $BaTiO_3$, for example, the ferroelectric distortion is induced by covalent interactions between the empty Ti 3d states and filled O 2p states, which lead to Ti^{4+} off-centering displacements within the oxygen octahedra.[7]

S. Yoshida, Prof. K. Fujita, T. Kuge, R. Tsuji, Dr. S. Murai, Prof. K. Tanaka
Department of Material Chemistry
Graduate School of Engineering
Kyoto University
Katsura Nishikyo-ku, Kyoto 615-8510, Japan
E-mail: fujita.koji.5w@kyoto-u.ac.jp

Dr. H. Akamatsu, Dr. A. S. Gupta, F. G. Brown, H. Padmanabhan, Prof. V. Gopalan
Materials Research Institute and Department of Materials Science and Engineering
Pennsylvania State University
University Park, PA 16802, USA

Dr. O. Hernandez
Univ Rennes
CNRS
ISCR (Institut des Sciences Chimiques de Rennes) - UMR 6226
F-35000 Rennes, France

Dr. A. S. Gibbs
ISIS Pulsed Neutron and Muon Source
STFC Rutherford Appleton Laboratory
Harwell Campus
OX11 0QX, UK

Prof. J. M. Rondinelli
Department of Materials Science and Engineering
Northwestern University
2220 Campus Drive, Evanston, IL 60208-3108, USA

Prof. V. Gopalan
Department of Physics
Pennsylvania State University
University Park, PA 16802, USA

The ORCID identification number(s) for the author(s) of this article can be found under https://doi.org/10.1002/adfm.201801856.

DOI: 10.1002/adfm.201801856

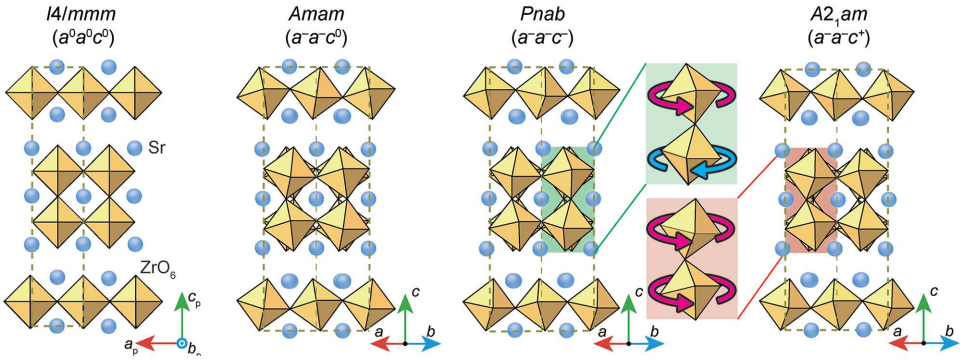

Figure 1. The crystal structures of four polymorphs observed experimentally in the present study are illustrated, specified by space group symmetry and Glazer tilt notation. Blue spheres and orange octahedra denote the Sr atoms and ZrO_6 octahedra, respectively, and green dotted rectangles indicate the unit cells.

Interestingly, Zr^{4+}-based simple perovskites, $AZrO_3$ (A = Ca, Sr, Ba, and Pb), are never ferroelectric even in the presence of d^0 (Zr^{4+})/$6s^2$ (Pb^{2+}) ions. For example, $CaZrO_3$, $SrZrO_3$, and $BaZrO_3$ are centrosymmetric paraelectric materials,[8–10] and stoichiometric $PbZrO_3$ is a centrosymmetric antiferroelectric material with T_C = 503 K.[11,12] This is presumably because the large energy gap between the Zr 4d states and O 2p states gives rise to insufficient dynamical charge transfer and covalency to overcome elastic energy costs. Upon chemical substitution with SOJT and SCALP ions in $PbZrO_3$, as in $PbZr_{1-x}Ti_xO_3$, ferroelectricity occurs, but the resulting Pb-based solid solutions are environmentally toxic. Thus, the achievement of ferroelectricity in valence precise ternary zirconates without chemical substitutions would propel ferroelectric research into new benign chemistries.

Here, we demonstrate that ferroelectricity emerges by layering[13–17] nonpolar perovskite $SrZrO_3$ with nonpolar rock salt-structured SrO to form the n = 2 Ruddlesden–Popper (RP) $A_3B_2O_7$ structure.[18] We show that $Sr_3Zr_2O_7$ is a hybrid improper ferroelectric (HIF), whereby ferroelectricity with an electric polarization P occurs from a combination of two nonpolar lattice modes, Q_1 and Q_2, interacting through a trilinear term of the form PQ_1Q_2.[19–31] The role played by the two nonpolar structural distortions—oxygen octahedral rotations (OOR, out-of-plane rotational modes) and oxygen octahedral tilts (OOT, in-plane rotational modes)—in stabilizing ferroelectricity is determined using a combination of synchrotron X-ray diffraction (SXRD), neutron powder diffraction (NPD), optical second harmonic generation (SHG), and first-principles density functional theory (DFT) calculations. Ferroelectric hysteresis measurements are performed to demonstrate room-temperature switchable electric polarizations in this ternary Pb-free zirconate. Variable-temperature structural analyses are used to identify the full sequence of temperature-induced phase transitions from the ferroelectric phase to the distortion-free aristotype phase. Most remarkably, we discover a metastable paraelectric polymorph (space group *Pnab*), which competes with the equilibrium ferroelectric phase ($A2_1am$), and an unusual first-order ferroelectric–paraelectric phase transition involving a change in the "sense" of the OOR while the OOT persists at all temperatures. We show that the paraelectric *Pnab* phase appears through a trilinear coupling of OOR and OOT modes interacting with an antipolar mode, a recently predicted hybrid improper "antiferroelectric" mechanism.[32,33] In addition to being of technological significance for the development of new ferroelectrics, our results highlight the importance of multimode anharmonic interactions in producing functional acentric material properties.

2. Results

2.1. Room-Temperature Ferroelectricity

The RP phases of general formula $AO(ABO_3)_n$ (or $A_{n+1}B_nO_{3n+1}$) have a layered structure where n ABO_3 perovskite blocks are stacked along the [001] direction, with an extra AO rock salt layer inserted for every n perovskite units (see **Figure 1** for n = 2).[18] Although n = 2 RP $Sr_3Zr_2O_7$ was previously reported to adopt a centrosymmetric *Pmmm* symmetry,[34] recent theoretical work and first-principles calculations indicated that $Sr_3Zr_2O_7$ is a potential HIF with $A2_1am$ symmetry.[35,36] We first characterized the room-temperature crystal structure of $Sr_3Zr_2O_7$ using SXRD and NPD. No impurities or secondary phases were detected in SXRD and NPD patterns.

Figure 2a shows the SXRD pattern at 300 K. The main reflections can be indexed with the tetragonal aristotype structure with space group $I4/mmm$, but we observed additional weak $h + 1/2\ k + 1/2\ l$ superlattice reflections (e.g., 3/2 3/2 3 reflection in **Figure 3**a), together with the splitting of basic hhl reflections (e.g., 110 reflection in Figure 3b). The superlattice reflections and reflection splittings are more clearly visible in the NPD data (Figure S1, Supporting Information). These results indicate that the room-temperature phase adopts an orthorhombic structure with an enlarged unit cell $\sqrt{2}\ a_p \times \sqrt{2}\ a_p \times c_p$ (where a_p and c_p are the pseudotetragonal lattice parameters), owing to the ZrO_6 OOR and/or OOT distortions.

The observed reflection conditions in the orthorhombic setting are hkl: $k + l = 2n$, $0kl$: $k + l = 2n$, $h0l$: $h, l = 2n$, $hk0$: $k = 2n$, $h00$: $h = 2n$, $0k0$: $k = 2n$, and $00l$: $l = 2n$ (n: integer). This allows us to propose $A2_1am$ (noncentrosymmetric polar) and *Amam* (centrosymmetric nonpolar) as the possible space groups ($Cmc2_1$ and *Cmcm* in standard setting, respectively). In the $A2_1am$ symmetry, out-of-phase OOT about [110] and in-phase OOR about [001] are allowed ($a^-a^-c^+$ in Glazer notation[37]),

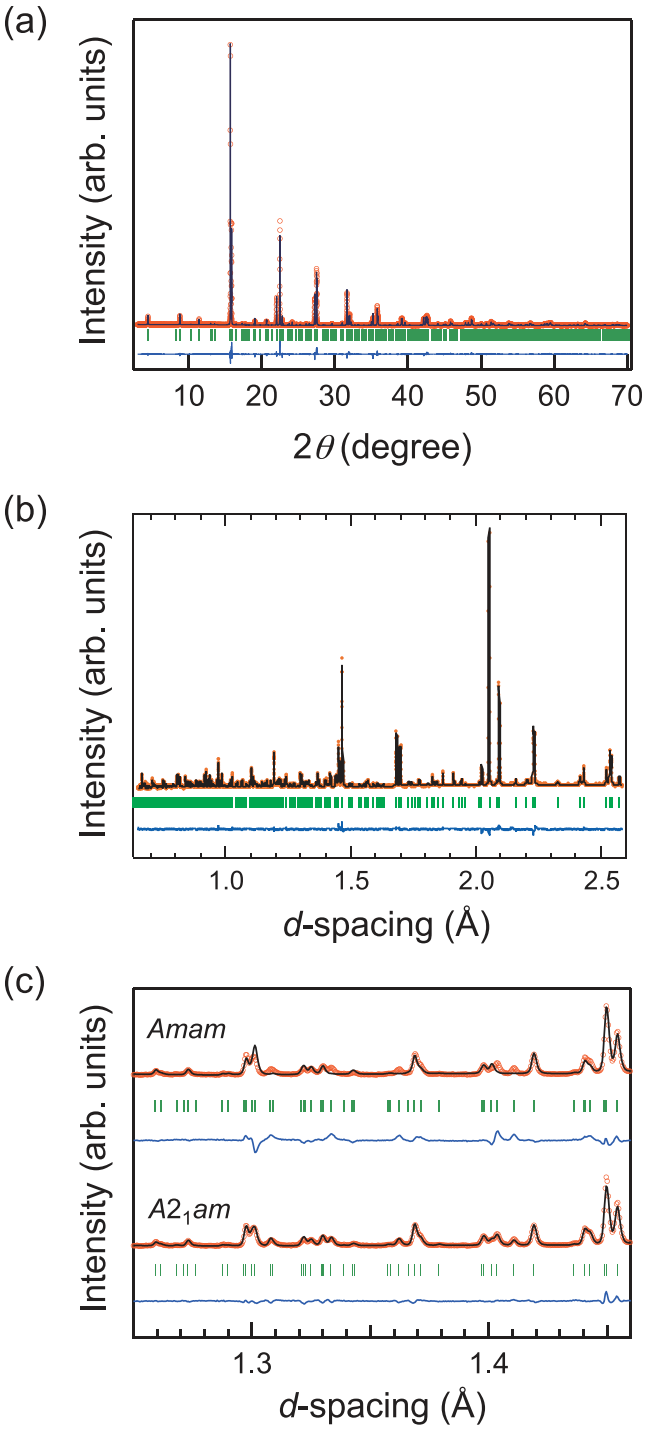

Figure 2. Rietveld refinement profiles with the polar structural model in orthorhombic $A2_1am$ symmetry against a) SXRD and b) NPD data at 300 K, showing observed (orange circles), calculated (black line), and difference (blue line) profiles. Green ticks indicate the position of Bragg reflections. c) Enlarged view of the Rietveld refinements with polar $A2_1am$ and nonpolar *Amam* models against NPD data at 300 K.

whereas only out-of-phase OOT about [110]—and no in-phase OOR about [001]—is allowed within the *Amam* symmetry ($a^-a^-c^0$). SXRD Rietveld refinements with $A2_1am$ and *Amam* models converge successfully, but the former model yields a significantly better fit (R_{wp} = 9.24%) than the latter model (R_{wp} = 12.8%).

Considering the fact that the $A2_1am$ structure can be distinguished from the *Amam* structure by in-phase OOR about [001], we also performed Rietveld refinements against the NPD data at 300 K (Figure 2b and Figure S2, Supporting Information), which provide much more accurate oxygen parameters than can be obtained from XRD. The polar $A2_1am$ model immediately provides a much better overall fit to the observed pattern (R_{wp} = 10.4%) than the *Amam* model (R_{wp} = 25.7%), and a detailed look at the refined pattern (Figure 2c) reveals a noticeable mismatch in some peak intensities for the *Amam* model. Our SXRD/NPD studies thus indicate that the room-temperature phase of $Sr_3Zr_2O_7$ belongs to polar $A2_1am$ space group; the structural refinement results are given in **Table 1**.

To corroborate the polar symmetry, we further measured optical SHG[38] and $P(E)$ hysteresis loop. These measurements are powerful tools to probe noncentrosymmetricity and ferroelectricity in materials. **Figure 4**a displays the temperature-dependent SHG intensity on heating and cooling cycles. A finite SHG signal, indicative of a noncentrosymmetric structure, is clearly observed around 300 K. This result, together with the SXRD/NPD analyses, allows us to unambiguously conclude that the room-temperature phase crystallizes in the polar $A2_1am$ structure. The ferroelectric nature is confirmed by the existence of clear $P(E)$ hysteresis loops (Figure 4b), measured using the remnant hysteresis method. The net remnant electric polarization and coercive electric field are ≈0.3 μC cm^{-2} and ≈150 kV cm^{-1}, respectively. The polarization value is comparable to those of polycrystalline $Ca_3Ti_2O_7$ (0.6 μC cm^{-2})[23] and $Sr_3Sn_2O_7$ (0.25 μC cm^{-2}),[24] but it is one order of magnitude smaller than that obtained from our DFT calculations (6.75 μC cm^{-2}). The smaller polarization value compared to the calculated one is expected from the polycrystalline nature. In fact, the polarization value of ≈0.6 μC cm^{-2} for polycrystalline $Ca_3Ti_2O_7$ is much smaller than that for single crystals (6.4 μC cm^{-2}).[25]

2.2. Temperature-Induced Phase Transitions

Having established that n = 2 RP $Sr_3Zr_2O_7$ is ferroelectric at 300 K, we next assess the ferroelectric phase transition. Figure 4a shows that the SHG intensity gradually decreases with increasing temperature and steeply drops to zero at a critical temperature (T_C) of ≈700 K, indicating the ferroelectric $A2_1am$ phase transforms into a centrosymmetric structure. The transition is accompanied by thermal hysteresis (≈50 K), which is determined from the variation in the SHG signals upon heating and cooling. These features together suggest a primarily first-order nature to the transition.

We also examined the displacive nature of the phase transformation near T_C ≈ 700 K using variable-temperature SXRD experiments. Upon heating across T_C, the orthorhombic $\sqrt{2}a_p \times \sqrt{2}a_p \times c_p$ unit cell remains unchanged as shown by the superlattice reflections (Figure 3a) and the orthorhombic splitting of the basic reflections (Figure 3b). Upon close inspection of the SXRD data, we find the appearance of new reflections around T_C and they persist up to 880 K as shown, for example,

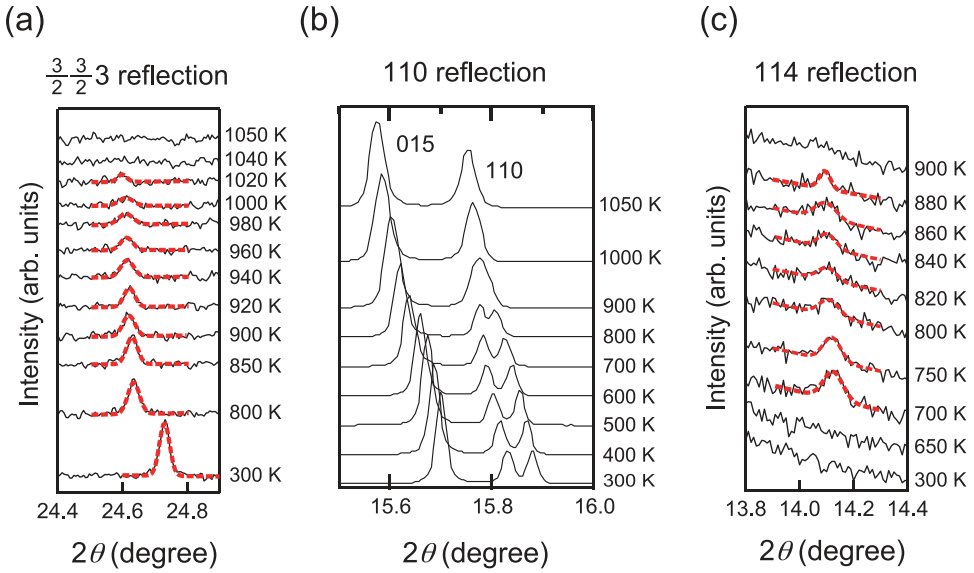

Figure 3. Temperature evolution of a) 3/2 3/2 3 superlattice reflection and b) basic 110 reflection. c) Temperature evolution of the 114 reflection, which is forbidden under the integral reflection condition of the *A*-centered orthorhombic lattice, but is allowed for the orthorhombic *P* lattice; the reflection is indexed by the $\sqrt{2}a_p \times \sqrt{2}a_p \times c_p$ cell.

for the 114 reflection displayed in Figure 3c. The 114 reflection is forbidden under the integral reflection condition of *A*-centered orthorhombic lattice (*hkl*: $k + l = 2n$), but is allowed for orthorhombic *P* lattice.

For phase identification, we utilized Aleksandrov's analysis of symmetry lowering in response to ZrO_6 OOR and OOT distortions in layered perovskites.[39] The centrosymmetric nonpolar phase explored here has the following characteristics: an even number of perovskite layers (i.e., $n = 2$), $I4/mmm$ in the absence of OOR and OOT, and a primitive orthorhombic $\sqrt{2}a_p \times \sqrt{2}a_p \times c_p$ cell. These conditions reduce the possible space groups to *Pnam*, *Pnab*, and *Pnnm* (*Pnma*, *Pbcn*, and *Pnnm* in the standard setting, respectively). Of these symmetries, a model refined in *Pnab*, involving the systematic absence for the *b*-glide plane, gives the only good fit to the 800 K SXRD data (**Figure 5**a and Figure S3, Supporting Information). More explicitly, refinements in the three space groups against the 750 K NPD data (Figure 5b and Figure S4, Supporting Information) and subsequent inspection of the refined patterns (Figure 5c) reveal some reflections that are accounted for in *Pnab* but not in *Pmcn* and *Pnnm*; R_{wp} = 11.7, 17.3, and 19.5% for *Pnab*, *Pmcn*, and *Pnnm*, respectively. These analyses support the assignment of the orthorhombic *Pnab* model as the paraelectric structure for $700 \leq T \leq 880$ K; the structural refinement results are given in **Table 2**. Although the out-of-phase OOT about [110] is present in both ferroelectric $A2_1am$ ($a^-a^-c^+$) and paraelectric *Pnab* ($a^-a^-c^-$) structures, there is a marked change in the sense of OOR about [001] across the $A2_1am$-to-*Pnab* phase transition (see Figure 1); the in-phase OOR in the $A2_1am$ phase vanishes and the out-of-phase OOR appears in the *Pnab* phase. The structural transformation accompanied by the change in OOR sense should occur discontinuously; indeed, there is no group–subgroup relationship between $A2_1am$ and *Pnab* (Figure S9, Supporting Information). Similar to the temperature hysteresis of SHG intensity in the vicinity of T_C (≈700 K) (Figure 4a), the discontinuous nature of the ferroelectric phase transition is confirmed by the temperature evolution of the SXRD patterns upon heating and cooling with fine-temperature interval sampling across T_C. An SXRD contour plot of the temperature-dependent $A2_1am$ 0010 and *Pnab* 0010 reflections (**Figure 6**a) illustrates this behavior. The $A2_1am$ and *Pnab* phases coexist over a wide

Table 1. Structural parameters obtained from refinements with an $A2_1am$ model against 300 K SXRD and NPD data.

SXRD					
Atom	Site	*x*	*y*	*z*	U_{iso} [Å^2]
O1	4*a*	0.2392(12)	0.796(3)	0	0.017(2)
O2	8*b*	0.2608(12)	0.6923(18)	0.1961(3)	= U_{iso}(O1)
O3	8*b*	0.5317(9)	0.5362(10)	0.0877(3)	0.012(2)
O4	8*b*	0.4683(9)	0.0362(10)	0.1084(4)	= U_{iso}(O3)
Sr1	4*a*	0.2644(14)	0.2478(11)	0	0.0160(7)
Sr2	8*b*	0.7379(8)	0.7432(5)	0.19017(4)	0.0076(4)
Zr	8*b*	0.75[a)]	0.2489(7)	0.09868(5)	0.0032(3)
NPD					
Atom	Site	*x*	*y*	*z*	U_{iso} [Å^2]
O1	4*a*	0.2382(16)	0.8116(8)	0	0.0104(12)
O2	8*b*	0.2623(13)	0.6941(5)	0.19710(10)	0.0093(8)
O3	8*b*	0.5338(14)	0.5328(6)	0.08608(10)	0.0077(7)
O4	8*b*	0.4658(13)	0.0321(7)	0.10892(12)	0.0113(8)
Sr1	4*a*	0.2677(16)	0.2515(8)	0	0.0090(10)
Sr2	8*b*	0.7344(10)	0.7407(5)	0.18951(7)	0.0093(7)
Zr	8*b*	0.75[a)]	0.2492(6)	0.09917(9)	0.0024(5)

Space group; $A2_1am$ (No. 36), $Z = 4$. The occupancy parameter is fixed to unity for all atoms. [a)]Fixed to define an origin of the polar *a*-axis. SXRD: cell parameters $a = 5.79933(6)$ Å, $b = 5.81707(6)$ Å, and $c = 20.9488(2)$ Å; $R_{wp} = 9.248\%$, $R_B = 3.429\%$, and $\chi^2 = 5.39$. NPD: cell parameters $a = 5.80175(10)$ Å, $b = 5.81979(10)$ Å, and $c = 20.9525(3)$ Å; $R_{wp} = 10.4\%$, $R_B = 4.54\%$, and $\chi^2 = 4.70$.

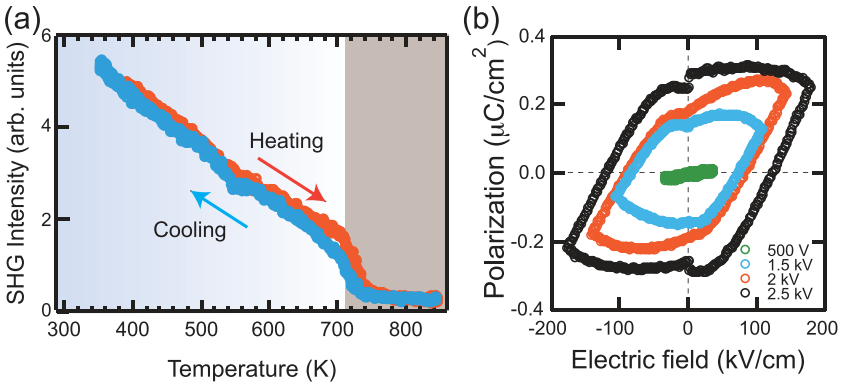

Figure 4. a) Temperature dependence of SHG intensity upon heating (orange line) and cooling (blue line). b) $P(E)$ hysteresis loops at room temperature for a bulk $Sr_3Zr_2O_7$ sample. The electric field was applied at frequency of 50 Hz.

temperature range (640–720 K), with a substantial hysteresis (≈50 K) on heating and cooling (Figure 6b). The unit cell volume also displays an obvious discontinuity across the transition region (Figure S7, Supporting Information). The overall results conclusively demonstrate the first-order nature of the ferroelectric phase transition. Moreover, our SXRD measurements confirmed that this transition is completely reversible. To the best of our knowledge, a first-order ferroelectric phase transition involving a change in the OOR sense is unreported. As discussed below, the unexpected appearance of the paraelectric *Pnab* phase as a high-temperature polymorph is due to strong anharmonic interactions among the lattice degrees of freedom.

Finally, we examine the phase transitions above the ferroelectric transition, $T_C \approx 700$ K, using variable-temperature SXRD experiments. As the temperature is increased from T_C, the 114 reflection from the *Pnab* phase vanishes at 900 K (Figure 3c), indicating a change in translational symmetry from a *P* lattice to either *A*- or *I*-centered lattice. On the other hand, the superlattice reflections (Figure 3a), as well as the orthorhombic splitting of basic reflections (Figure 3b), are still visible at 900 K; such features disappear completely around 1040 K above which the sample adopts the tetragonal aristotype $I4/mmm$ structure. These results reveal that the orthorhombic *Pnab* phase transforms to the tetragonal $I4/mmm$ phase via an intermediate orthorhombic phase with an *A*-centered lattice ($900 \leq T \leq 1040$ K). Given the nonpolar character of the intermediate phase, its space group is uniquely determined as *Amam*. Details of the structural refinements with *Amam* and $I4/mmm$ models are presented in Section S4 (Supporting Information).

Thus, the sequence of phase transitions upon heating above T_C is best described as *Pnab* ($a^-a^-c^-$) → *Amam* ($a^-a^-c^0$) → $I4/mmm$ ($a^0a^0c^0$), where the out-of-phase OOR is first lost in the second-order displacive *Pnab* → *Amam* transition and then the out-of-phase OOT is lost in the second-order displacive *Amam* → $I4/mmm$ transition (see also the group–subgroup relationship in Figure S9, Supporting Information). Indeed, the unit cell volume does not show any discontinuity across the two transitions (Figure S7, Supporting Information), which is typical for a second-order phase transition. Note that upon heating up to 1050 K, there is no sign of any thermal degradation or decomposition in the SXRD patterns, indicating the high thermal stability of the zirconate.

Our structural studies combined with physical property measurements uncover symmetry-lowering phase transitions of $n = 2$ RP $Sr_3Zr_2O_7$ from the aristotype $I4/mmm$ phase to the ferroelectric $A2_1am$ ground state. The phase diagram is depicted in **Figure 7**; for reference, the OOR/OOT patterns of the observed four phases are shown in the lower part of the figure.

2.3. DFT Calculations

To identify the structural distortions driving this system into the ferroelectric $A2_1am$ phase, we performed first-principles calculations of the lattice dynamics and energetics. We first calculated the phonon dispersion curves in the distortion-free $I4/mmm$ phase (**Figure 8**a) so that the symmetry-reducing and energy-lowering atomic displacement patterns can be identified. Numerous instabilities are found throughout the Brillouin zone. We now focus on the instabilities at the Γ, X, and M points, which produce frequently observed hettotype phases in perovskite-derived structures. Along the Γ–*X* direction, we find a pair of doubly degenerate unstable (imaginary-frequency) modes at the Γ point and eight unstable modes at the X point. The manifold of unstable phonon modes indicates that numerous displacement modes can lower the energy of the $I4/mmm$ phase. If we first consider the condensation of each mode individually, then the unstable mode that drives the largest energy gain occurs at the zone-boundary (X point). This mode is a ZrO_6 OOT, which corresponds to an out-of-phase OOT about [110] (transforming as the irreducible representation [irrep] X_3^-) and generates the centrosymmetric *Amam*, $P4_2/mnm$, and *Pnnm* phases. The zone-boundary instabilities involving ZrO_6 OOR about [001] (e.g., irreps X_2^+ and X_1^-) also give significant energy gains. Also, there exist zone-center polar instabilities at the Γ point (irrep Γ_5^-). The unstable Γ_5^- normal modes provide a very minor contribution to the polar $A2_1am$ phase for the following two reasons (see also Section S9, Supporting Information, for details): (1) the displacement patterns of the unstable Γ_5^- modes are represented by the parallel Sr cation displacements in $n = 2$ perovskite slabs comprising the RP structure, that is, *ferroelectric* distortions, in contrast to the *ferrielectric*[40] Γ_5^- distortion in the experimental $A2_1ma$ phase (as shown in the next section), and (2) these *ferroelectric* Γ_5^- modes become harder by condensing both the X_2^+ and X_3^- modes. Thus, $Sr_3Zr_2O_7$ is not a proper ferroelectric. When considering the condensation of more than one unstable modes, we find that several low-symmetry phases of similar energy can be obtained. For example, condensing the X_2^+ (OOR) and X_3^- (OOT) modes together ($A2_1am$ and *Pnam*) gives an energy gain similar to that obtained by condensing the X_1^- (OOR) and X_3^- (OOT) modes together (*Pnab* and $A2/a$). For this reason, we repeated a sequential process of including the condensation of identified unstable modes, structural optimization, and phonon calculations up to the point where no unstable mode remained

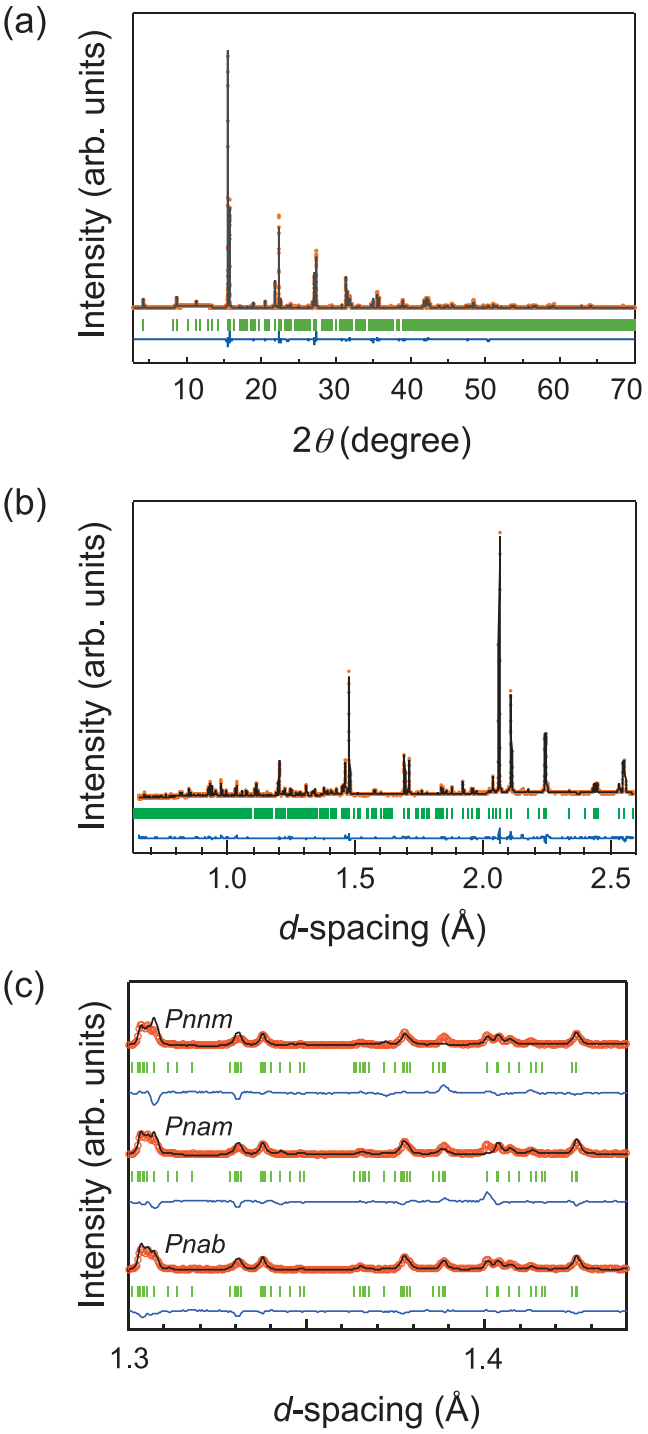

Figure 5. Rietveld refinement profiles for a) 800 K SXRD and b) 750 K NPD data fitted with *Pnab* model. c) Enlarged view of the Rietveld refinements with *Pnnm*, *Pnam*, and *Pnab* models against NPD data at 750 K. Orange circles and black and blue lines represent the observed, calculated, and difference profiles, respectively. The green ticks show the position of Bragg reflections.

in the structure to find the lowest-energy polymorphs. As shown in **Table 3** and Figure S8 (Supporting Information), the systematic stable-structure exploration reveals the polar $A2_1am$ phase to be the most stable, consistent with our experimental observation and previous first-principles investigation,[35,36] and it also uncovers many possible metastable phases. We next calculated the energy surface around the aristotype $I4/mmm$ phase using DFT to identify the role of the OOR and OOT modes in stabilizing the ground-state $A2_1am$ phase. We projected the calculated structural distortion bringing the $I4/mmm$ to $A2_1am$ phases onto the three symmetry-adapted modes, X_3^-, X_2^+, and Γ_5^- modes, which have isotropy subgroups *Amam*, *Acam*, and *F2mm*, respectively. In Figure 8b, we show the total energy as a function of X_2^+ (OOR) and X_3^- (OOT) mode amplitudes, $Q_{X_2^+}$ and $Q_{X_3^-}$. As expected, large energy gains are observed within a double-well potential for both the modes. The importance of the coupling between $Q_{X_2^+}$ and $Q_{X_3^-}$ can be seen by plotting the total energy as a function of Γ_5^- mode amplitude, $Q_{\Gamma_5^-}$, with $Q_{X_2^+}$ and $Q_{X_3^-}$ fixed (Figure 8c). Note that the Γ_5^- mode appears as a *ferrielectric* mode characterized mainly by two-against-one Sr cation displacements in the $n = 2$ perovskite slabs (Section S9, Supporting Information), consistent with our experimental results of layer-resolved electric polarizations (see the next section). All the energy surfaces exhibit single-well parabolas with minima at $Q_{\Gamma_5^-} = 0$ except when both $Q_{X_2^+}$ and $Q_{X_3^-}$ are finite; only in the simultaneous presence of $Q_{X_2^+}$ and $Q_{X_3^-}$ does the energy surface exhibit a minimum at $Q_{\Gamma_5^-} \neq 0$. Thus, we find that the polar Γ_5^- distortion is energetically favored via a trilinear coupling, $Q_{\Gamma_5^-}Q_{X_3^-}Q_{X_2^+}$. This polar Γ_5^- mode becomes softer by condensing both the X_2^+ and X_3^- modes (Figure 8c). The overall behavior indicates that the ZrO_6 OOR and OOT are the primary structural distortions driving the transition to the

Table 2. Structural parameters obtained from refinements with a *Pnab* model against 800 K SXRD and 750 K NPD data.

SXRD					
Atom	Site	x	y	z	U_{iso} [Å^2]
O1	4*a*	0.75	0.727(6)	0	0.040(20)
O2	8*b*	0.959(3)	0.046(3)	0.9088(4)	0.024(2)
O3	8*b*	0.733(4)	0.786(3)	0.8041(3)	$= U_{iso}$(O2)
O4	8*b*	0.015(4)	0.017(3)	0.6043(4)	$= U_{iso}$(O1)
Sr1	4*a*	0.75	0.253(15)	0	0.0273(5)
Sr2	8*b*	0.75(12)	0.2458(8)	0.81015(4)	0.0203(4)
Zr	8*b*	0.7503(8)	0.7508(9)	0.90119(4)	0.0093(2)
NPD					
Atom	Site	x	y	z	U_{eq} or U_{iso} [Å^2]
O1	4*a*	0.75	0.7161(2)	0	0.043(5)[a)]
O2	8*b*	0.974(12)	0.0252(10)	0.91104(13)	0.0249(14)
O3	8*b*	0.752(2)	0.7873(10)	0.80250(13)	0.037(3)[a)]
O4	8*b*	0.032(13)	0.0313(9)	0.60535(17)	0.0256(16)
Sr1	4*a*	0.75	0.2508(18)	0	0.028(3)[a)]
Sr2	8*b*	0.751(19)	0.2406(10)	0.81053(8)	0.026(3)[a)]
Zr	8*b*	0.751(19)	0.7503(9)	0.90106(10)	0.0104(13)[a)]

Space group; *Pnab* (No. 60), $Z = 4$. The occupancy parameter is fixed to unity for all atoms. [a)]Refined anisotropically. SXRD: cell parameters $a = 5.82641(6)$ Å, $b = 5.83834(6)$ Å, and $c = 21.0838(2)$Å; $R_{wp} = 8.36\%$, $R_B = 2.47\%$, and $\chi^2 = 5.37$. NPD: cell parameters $a = 5.82437(11)$ Å, $b = 5.83868(11)$ Å, and $c = 21.0784(4)$ Å; $R_{wp} = 11.7\%$, $R_B = 6.11\%$, and $\chi^2 = 3.38$.

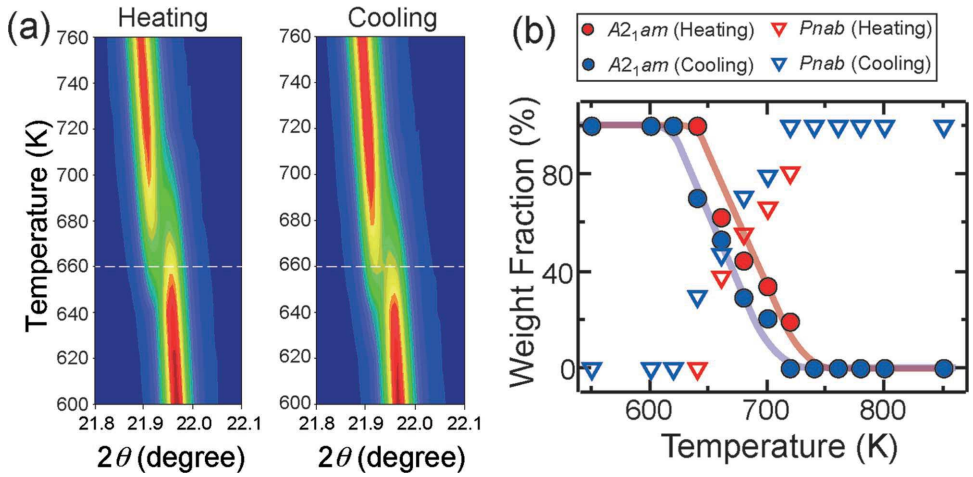

Figure 6. a) Contour plot of the temperature dependence of SXRD 0010 reflection upon heating and cooling across the ferroelectric transition between the polar $A2_1am$ and nonpolar *Pnab* phases. b) Temperature evolution of the weight fraction of two phases ($A2_1am$ and *Pnab*) coexisting in the ferroelectric–paraelectric phase transition. The weight fraction was calculated by using a multiphase Rietveld refinement against SXRD data.

polar $A2_1am$ phase and that the ferrielectric Sr displacements play a secondary role in stabilizing the polar phase. Thus, we assess the importance of trilinear coupling between the order parameters of the three relevant modes in $Sr_3Zr_2O_7$, proving it to be a HIF.

3. Discussion

3.1. Experimental Verification of the Hybrid Improper Ferroelectricity

The atomistic origin of the ferroelectric polarization in $Sr_3Zr_2O_7$ is identified by investigating the layer-resolved electric polarizations of the experimental polar $A2_1am$ structure. The layer-resolved polarization estimated from the NPD-refined structure is shown in **Figure 9**a. One can see that the polarization mainly results from a noncancellation of the layer polarizations (i.e., ferrielectric mechanism) induced by the in-plane *A*-site cation (Sr^{2+} in this case) displacements along [100] (Figure S10, Supporting Information), like in HIF $Ca_3Ti_2O_7$[21,23,25] and $Ca_3Mn_2O_7$.[21] Although the B-site cation (Zr^{4+}) displacements also produce a layer polarization along [100], its contribution to the total polarization is vanishingly small, indicating that a proper SOJT mechanism, that is, dynamical charge transfer between the Zr 4d states and O 2p states, plays a minor role in stabilizing the polar structure. This is in striking contrast to $Ca_3Ti_2O_7$ where the d(Ti)–p(O) charge transfer enhances the polarization arising from the B–O layers (Figure S11, Supporting Information). In terms of the small Zr–O layer polarization, the behavior of layer-resolved polarizations for $Sr_3Zr_2O_7$ is more similar to that for $Ca_3Mn_2O_7$ (Figure S11, Supporting Information), where proper ferroelectricity is difficult to be realized because of the d^3 electronic configuration of Mn^{4+}. Therefore, we suggest that the polar instability in $Sr_3Zr_2O_7$ is driven purely by OOR and OOT

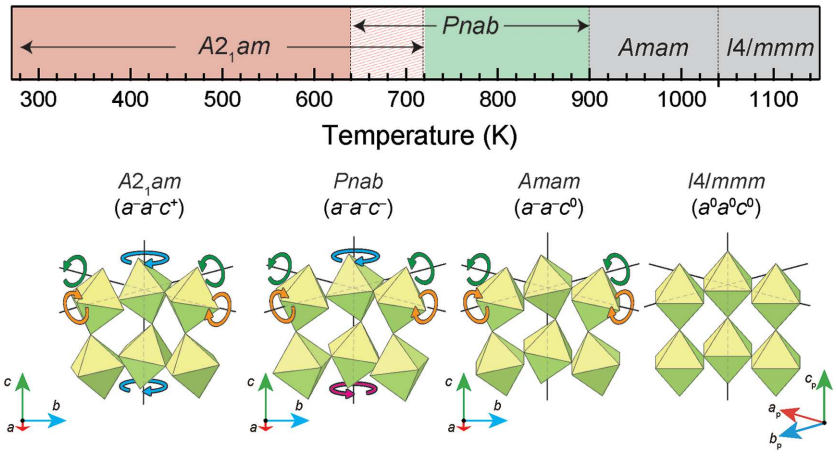

Figure 7. Polymorphic phase diagram of $Sr_3Zr_2O_7$ established by the diffraction studies combined with SHG. The OOR/OOT patterns of the observed four phases are highlighted in the lower part. Arrowed arcs depict the sense of OOR (red and blue) and OOT (green and orange).

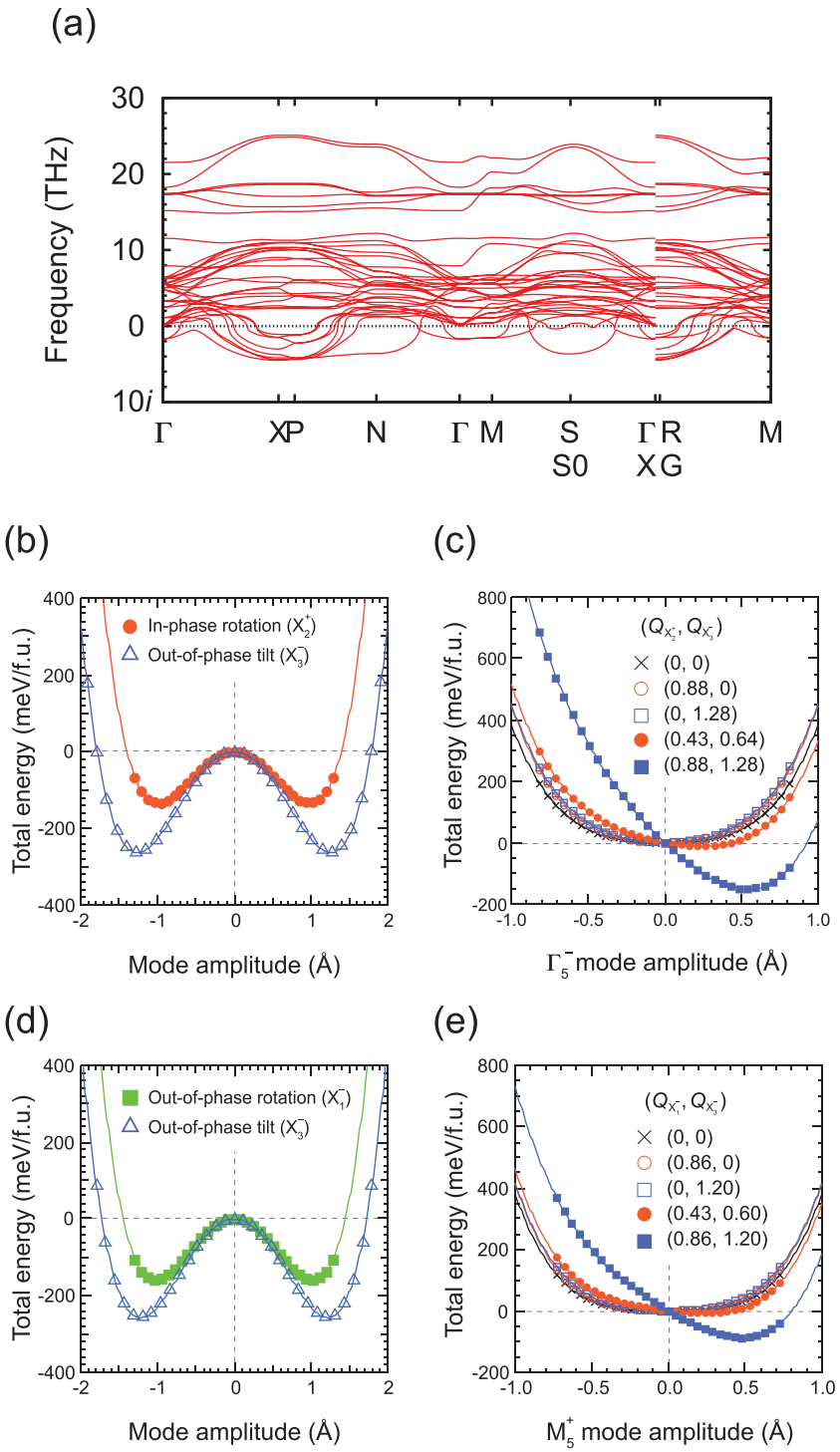

Figure 8. a) Calculated phonon dispersion curves for the aristotype $I4/mmm$ phase of $Sr_3Zr_2O_7$. Imaginary frequencies correspond to unstable phonon modes. b) Total energy as a function of the amplitude of X_2^+ (in-phase OOR) and X_3^- (out-of-phase OOT) modes, $Q_{X_2^+}$ and $Q_{X_3^-}$. c) Total energy as a function of the amplitude of polar Γ_5^- mode, $Q_{\Gamma_5^-}$, for various sets of $Q_{X_3^-}$ (Å) and $Q_{X_2^+}$ (Å). Note that the polar Γ_5^- mode corresponds to the ferrielectric mode, leading to a noncancellation of the layer polarizations along [100] (Figure S10 and Section S9, Supporting Information). d) Total energy as a function of the amplitude of X_1^- (out-of-phase OOR) and X_3^- (out-of-phase OOT) modes, $Q_{X_1^-}$ and $Q_{X_3^-}$. e) Total energy as a function of the amplitude of antipolar M_5^+ mode, $Q_{M_5^+}$, for various sets of $Q_{X_3^-}$ (Å) and $Q_{X_1^-}$ (Å). The antipolar M_5^+ mode results in a complete cancellation of the layer polarizations along [100] (Figure S10, Supporting Information).

distortions, which, together with the layered topology of the RP structure, lead to inversion symmetry breaking and the appearance of an electric polarization.

The nature of hybrid improper ferroelectricity in the polar $A2_1am$ phase is also corroborated experimentally by the temperature evolution of the SHG intensity, I_{SHG}, and the hybrid order parameter, $\eta = Q_{X_2^+}Q_{X_3^-}$, between 300 and 600 K (Figure 9b). The diagnostics with SHG is based on the sensitivity of SHG intensity to the order parameter, and hence, the temperature dependence of the square root of SHG intensity, $\sqrt{I_{SHG}}$, typically follows the $P(T)$ behavior. The η values are determined through a symmetry-mode analysis of the experimental (NPD-refined) structures using the AMPLIMODES software.[41] As expected from the trilinear coupling mechanism, $\sqrt{I_{SHG}}$ is observed to change continuously with temperature in proportion to η.

3.2. Competition between Hybrid Improper Ferroelectric and Antiferroelectric Mechanisms

The experimental signature of the first-order ferroelectric-to-paraelectric ($A2_1am$-to-$Pnab$) transition (Figure 6), which manifests microscopically as a change in the "sense" of OOR while keeping the OOT mode (see Figures 1 and 7), clearly indicates that the structural instabilities leading to the ferroelectric $A2_1am$ phase compete with those leading to the paraelectric $Pnab$ polymorph. In several metastable phases obtained from our theoretical stable-structure exploration, the $Pnab$ polymorph is one of the most stable phases and has only a slightly higher energy (18 meV per formula unit) than the equilibrium ferroelectric $A2_1am$ phase. Using DFT calculations, we further examine the role of the OOR and OOT modes in stabilizing the $Pnab$ structure. The distortion that relates the aristotype $I4/mmm$ phase to the $Pnab$ phase can be decomposed into the symmetry-adapted modes as follows: out-of-phase OOR about [001] (X_1^-), out-of-phase OOT about [110] (X_3^-), and in-plane antipolar displacement modes along [100] (M_5^+). The energetics of these structural distortions shows that the X_1^- (OOR) and X_3^- (OOT) modes lower the energy of the aristotype structure (Figure 8d) and that the antipolar M_5^+ mode only lowers the energy in the simultaneous presence of the X_1^- and X_3^- modes (Figure 8e). This is a manifestation of a trilinear coupling, $Q_{M_5^+}Q_{X_1^-}Q_{X_3^-}$,

Table 3. Low-energy structures arising from oxygen octahedral rotation and/or tilt modes obtained by systematic structure exploration.

Space group[a)]	Total energy[b)] [meV f.u.$^{-1}$]	irrep[c)]
Abaa (No. 68)	−275	X_1^- (*a*, 0)
Acam (No. 64)	−239	X_2^+ (*a*, 0)
Amam (No. 63)	−332	X_3^- (*a*, 0)
$P4_2/mnm$ (No. 136)	−353	X_3^- (*a*, *a*)
$P4_2/mcn$ (No. 132)	−223	X_4^- (*a*, *a*)
Acmm (No. 67)	−187	X_4^- (*a*, 0)
Pnnm (No. 58)	−353	X_3^- (*a*, *b*)
Pbcm (No. 57)	−295	$X_2^+ \oplus X_4^-(a,0;b,0)$
$A2_1am$ (No. 36)	−395	$X_2^+ \oplus X_3^-(a,0;b,0)$
Pnam (No. 62)	−387	$X_2^+ \oplus X_3^-(0,a;b,0)$
*A*2/*a* (No. 15)	−368	$X_1^- \oplus X_3^-(a,0;b,0)$
Pnab (No. 60)	−377	$X_1^- \oplus X_3^-(0,a;b,0)$
*B*2*cm* (No. 39)	−305	$X_2^+ \oplus X_4^-(a,0;b,0)$
*P*2/c (No. 13)	−298	$X_1^- \oplus X_4^-(a,0;b,0)$
Pbcb (No. 54)	−308	$X_1^- \oplus X_4^-(0,a;b,0)$
*A*2/*m* (No. 12)	−338	$X_3^- \oplus X_4^-(a,0;b,0)$
$P2_1nm$ (No. 31)	−363	$X_2^+ \oplus X_3^-(a,0;b,c)$

[a)]The first column displays the space group of the low-energy structure; [b)]The second column shows the total energy with respect to the aristotype *I*4/*mmm* structure; [c)]The third column lists the single irrep with order parameter direction (η_1, η_2) (upper rows) and the coupled irrep with order parameter direction (η_1, η_2; η_3, η_4) (lower rows). These irreps were condensed into the aristotype *I*4/*mmm* structure, giving the isotropy subgroups shown in the first column. Note that the inequivalent order parameter directions for an irrep lead to the distinct structures; for example, X_3^- condensations give rise to *Amam* for (*a*, 0), *Pnnm* for (*a*, *b*), and $P4_2/mnm$ for (*a*, *a*).

and makes the *Pnab* phase a hybrid improper "antiferroelectric"; the antipolar mode leads to a complete cancellation of the layer polarizations along [100], providing no net macroscopic polarization (Figure S10, Supporting Information). Note in Table 3 that the *Pnam* phase is the second most stable polymorph, lying only 8 meV per formula unit above the ground-state $A2_1am$ phase. The *Pnam* as well as $A2_1am$ structures are induced by the coupled irrep ($X_2^+ \oplus X_3^-$), and the OOR/OOT patterns in both the structures are represented by $a^-a^-c^+$. The *Pnam* structure can be distinguished from the $A2_1am$ structure through the relative rotation sense of OORs in adjacent $n = 2$ perovskite blocks; $a^-a^-c^+/a^-a^-c^+$ for $A2_1am$ and $a^-a^-c^+/a^-a^-(-c^+)$ for *Pnam*.[14] For the *Pnam* phase, the two-against-one Sr cation displacements in adjacent perovskite blocks are in opposite direction, making the crystal structure centrosymmetric and antipolar. The low-energy antipolar *Pnam* structure was not experimentally observed through our SXRD and NPD structural analysis on polycrystalline samples, but should be present as a "stacking domain wall" in a multidomain $A2_1am$ matrix as discussed previously.[42]

We also extracted X_2^+, X_3^-, and Γ_5^- (X_1^-, X_3^-, and M_5^+) modes from a fully relaxed $A2_1am$ (*Pnab*) structure and calculated the total energies of the structures obtained by freezing each of the three extracted modes or their combinations (**Figure 10**). Relatively large energy gains are obtained through the trilinear coupling interactions in $A2_1am$ and *Pnab* phases. Remarkably, the trilinear coupling interaction in the *Pnab* phase, $Q_{M_5^+}Q_{X_1^-}Q_{X_3^-}$, competes with that in the $A2_1am$ phase, $Q_{\Gamma_5^-}Q_{X_2^+}Q_{X_3^-}$, that is, there is a delicate balance between hybrid improper ferroelectricity and antiferroelectricity. Thus, the unusual ferroelectric phase transition in $Sr_3Zr_2O_7$ is understood to occur from the interplay between the multimode anharmonic interactions active in the layered oxide. The form of hybrid improper "antiferroelectricity," $Q_{M_5^+}Q_{X_1^-}Q_{X_3^-}$, was recently predicted by first-principles calculations,[32,33] but has not been demonstrated experimentally. Our results represent the first experimental verification corroborating this prediction, and show the importance of understanding anharmonic interactions among lattice degrees of freedom using state-of-the-art X-ray and neutron diffraction as well as nonlinear optical methods.

4. Conclusion

In summary, we demonstrate that $n = 2$ RP $Sr_3Zr_2O_7$ is an ideal hybrid improper ferroelectric, for which a proper mechanism, that is, d(Zr)–p(O) charge transfer, plays a minor role (or no role at all) in stabilizing the ferroelectric phase. Rather, the nonpolar OOR and OOT modes trilinearly couple to drive the system toward a stable ferroelectric state, making $Sr_3Zr_2O_7$ a chemically benign and robust room-temperature ferroelectric. This discovery should stimulate further detailed experimental investigations concerning domain structures and polarization switching and open routes to the possible use of hybrid improper ferroelectrics in real technological applications, including thermoelectric applications where competing phases and anharmonicities in the lattice dynamical properties can be exploited to control thermal conductivity. The approach presented here, that is, layering of nonpolar ternary systems, is generalizable to a wide range of materials and thus we expect that there would still exist many new classes of hybrid improper ferroelectrics in chemical-composition spaces that do not exhibit a proper ferroelectric mechanism.

Another aspect that deserves attention in the present study is the appearance of the antipolar *Pnab* structure as a high-temperature polymorph, which is stabilized by a hybrid improper "antiferroelectric" mechanism. We find theoretically and experimentally that the antipolar *Pnab* polymorph competes

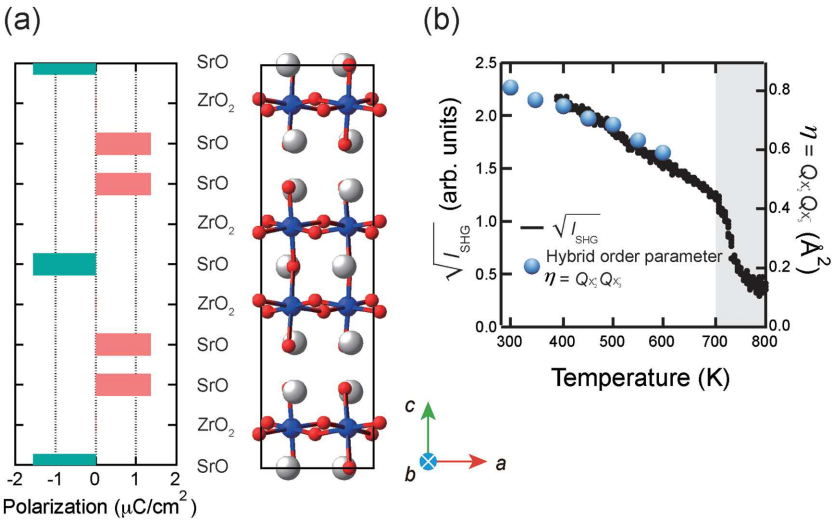

Figure 9. a) Layer-resolved polarization calculated using a point-charge approximation for the crystal structure refined against the NPD data at 300 K (Left panel). Right panel shows the [010] projected crystal structure with Sr, Zr, and O atoms in gray, blue, and red, respectively. The macroscopic polarization results from the noncancellation of the local polarization in the SrO layers; the contribution from the ZrO_2 layers is vanishingly small. b) Temperature evolution of the square root of SHG intensity, $\sqrt{I_{SHG}}$, and hybrid order parameter, $\eta = Q_{X_2^-}Q_{X_3^-}$, in the temperature range of the polar $A2_1am$ phase.

with the equilibrium polar $A2_1am$ phase. An interesting direction for possible future investigations is understanding how to control the relative energetics of these two structures. In this respect, it will be interesting to explore experimentally the possibility of epitaxial-strain-induced polar-to-nonpolar ($A2_1am$-to-$Pnab$) transition, according to the recent theoretical prediction.[32,33] The synthesis routes, annealing conditions, and cation substitutions should also activate new modes through the change in OOT and OOR preferences. Such future studies could help to evaluate the relationship between hybrid improper ferroelectricity and hybrid improper antiferroelectricity and provide a pathway to find new antiferroelectrics, which would be of both fundamental and technological interest.[43,44]

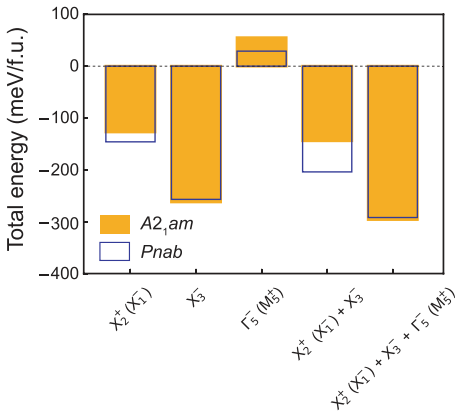

Figure 10. Energetic contributions from freezing of the distortion modes in the $A2_1am$ and $Pnab$ phases.

5. Experimental Section

Polycrystalline samples of $Sr_3Zr_2O_7$ were synthesized by the conventional solid-state reaction. Stoichiometric amount of reagent-grade $SrCO_3$ (99.9%, Kojundo Chemical Laboratory Co., Ltd.) and ZrO_2 (99.9%, Kishida Chemical Co., Ltd.) were mixed and ground in an agate mortar. The mixed powder was calcinated at 1000 °C for 12 h and sintered at 1500 °C for 48 h. They were slowly cooled to room temperature.

Variable-temperature SXRD data were recorded in the temperature range of 300–1050 K by using the large Debye–Scherrer camera, installed at SPring-8 BL02B2 of JASRI. The incident beam from a bending magnet was monochromated at λ = 0.798833 Å. The minimum d value reached was as low as 0.697 Å. The powder sample was loaded into a Lindemann capillary tube with an inner diameter of 0.1 mm (300 K ≤ T ≤ 800 K) and a silica capillary tube with an inner diameter of 0.2 mm (800 K ≤ T ≤ 1050 K), which were rotated continuously during measurement to diminish the effect of preferred orientation. The structural parameters were refined by the Rietveld method[45] with RIETAN-FP program.[46] Variable-temperature time-of-flight NPD was performed in the temperature range of 300–750 K using the HRPD diffractometer at the ISIS facility, UK. ≈5 g of powder sample was housed in a cylindrical vanadium can, which was mounted in a standard vacuum furnace for high-temperature data collection. Data were collected in two time-of-flight windows (30–130 and 100–200 ms), allowing cleanly catching the observable Bragg reflections in the d range of 0.65–11.6 Å with a high resolution and satisfactory counting statistics. Backscattering bank (centered on 2θ = 168°), 90° bank (centered on 2θ = 90°), and low angle bank (centered on 2θ = 30°) data were used for refinement. The structural parameters were refined by the Rietveld method[45] with the FullProf suite.[47]

Optical SHG measurements were performed with an 800 nm beam emitted from Ti:sapphire laser (80 fs pulse, 1 kHz repetition rate) in reflection geometry. Electric polarization versus electric field (P–E) hysteresis was measured with a ferroelectric tester (Precision LC, Radiant Technologies) and a high-voltage amplifier (10 kV HVI-SC, Radiant Technologies). In the measurements, high-density pellets (99.8%) prepared by spark plasma sintering method (LABOX 125GH, Sinterland) were used.

DFT calculations were carried out by employing the projector augmented wave (PAW) method[48,49] and PBEsol functional[50–52] as implemented in the VASP code.[53–56] Radial cutoffs in PAW data sets are 2.1, 1.6, and 0.8 Å for Sr, Zr, and O, respectively. A cutoff energy of 550 and 700 eV was used for plane waves when lattice parameters need to be optimized and when density functional perturbation theory (DFPT) calculations were performed, respectively. A cutoff energy of 400 eV was used otherwise. The following states were regarded as valence states: Sr 4s, 4p, and 5s; Zr 4s, 4p, 5s, and 4d; O 2s and 2p. We optimized lattice vectors and fractional coordinates until the residual stress and forces converged down to 0.01 GPa and 1 meV Å^{-1}, respectively. The Born effective charge tensor of atom s, Z^*_s, in the parent $I4/mmm$ structure was calculated based on DFPT, and the total electric polarization for the polar $A2_1am$ structure was derived from the following equation

$$P = \frac{e}{V}\sum_s Z_s^* u_s \quad (1)$$

where e is the elementary charge, V is the unit cell volume, and u_s is the displacement of atom s away from its position in the $I4/mmm$ structure.

The lattice dynamics calculations were done utilizing a frozen-phonon method as implemented in the PHONOPY code,[57] which generates atomic displacements necessary to calculate dynamical matrices

and diagonalize the matrices so as to provide phonon frequencies and corresponding eigenmodes. The phonon dispersion curves were drawn for a standard primitive cell[58,59] along a q-space path based on crystallography.[60] For systematic stable structure exploration,[61–63] phonon frequencies were calculated at the Brillouin zone center for a $\sqrt{2} \times \sqrt{2} \times 1$ supercell of the aristotype $I4/mmm$ conventional cell with a $4 \times 4 \times 1$ k-point mesh. We note that the zone-center phonon modes for the supercell include modes relevant to zone-boundary phonon modes at the X and M points for its primitive cell, due to band folding. We distorted the parent $I4/mmm$ structure according to the eigenvectors of the found unstable modes so as to obtain more stable structures with lower symmetry, and calculated phonon frequencies after optimizing well their structural parameters to see if there is any phonon instability. The cell size was fixed during the stable structure exploration.

For the energy surface calculations, structural distortions were decomposed into symmetry-adapted modes of the parent $I4/mmm$ phase using the AMPLIMODES tool available at the Bilbao Crystallographic Server.[41] The mode amplitude is defined as a square root of the sum of squared displacement vectors. The distortion patterns are visualized by the VESTA code.[64]

[Further details of the crystal structure investigation may be obtained from the Fachinformationszentrum Karlsruhe, 76344 Eggenstein-Leopoldshafen (Germany), on quoting the depository number CSD-434270.]

Supporting Information

Supporting Information is available from the Wiley Online Library or from the author.

Acknowledgements

The authors thank K. Miura and Y. Shimotsuma for use of spark plasma sintering equipment. This work was supported by the JSPS KAKENHI (Grant Nos. JP16H04496, JP16K14386, JP17H01320, and JP17K19172), the Murata Science Foundation, the Grant-in-Aid for JSPS Research Fellow (Grant No. JP17J07106), and National Science Foundation Grants numbers DMR-1729338 and DMR-1420620 (Penn State MRSEC Center for Nanoscale Science). SXRD experiments were performed on BL02B2 at SPring-8 with the approval of JASRI (Proposal Nos. 2016A1308, 2016B1269, and 2017A1357). Time-of-flight NPD experiments on HRPD at the ISIS Pulsed Neutron and Muon Source were supported by a beam time allocation from STFC (RB1620102).

Conflict of Interest

The authors declare no conflict of interest.

Keywords

antiferroelectrics, ferroelectrics, layered perovskites, oxygen octahedral rotations/tilts

Received: March 14, 2018
Revised: April 19, 2018
Published online: May 28, 2018

[1] M. Kohli, C. Wuethrich, K. Brooks, B. Willing, M. Forster, P. Muralt, N. Setter, P. Ryser, *Sens. Actuators, A* **1997**, *60*, 147.
[2] C.-B. Eom, S. Trolier-McKinstry, *MRS Bull.* **2012**, *37*, 1007.
[3] H. Kueppers, T. Leuerer, U. Schnakenberg, W. Mokwa, M. Hoffmann, T. Schneller, U. Boettger, R. Waser, *Sens. Actuators, A* **2002**, *97*, 680.
[4] R. E. Cohen, *Nature* **1992**, *358*, 136.
[5] N. A. Hill, *J. Phys. Chem. B* **2000**, *104*, 6694.
[6] I. B. Bersuker, *Phys. Rev. Lett.* **2012**, *108*, 137202.
[7] I. B. Bersuker, *Chem. Rev.* **2013**, *113*, 1351.
[8] H. J. A. Koopmans, G. M. H. Van De Velde, P. J. Gellings, *Acta Crystallogr., Sect. C: Struct. Chem.* **1983**, *39*, 1323.
[9] A. Ahtee, M. Ahtee, *Acta Crystallogr., Sect. B: Struct. Sci., Cryst. Eng. Mater.* **1976**, *32*, 3243.
[10] I. Levin, T. G. Amos, S. M. Bell, L. Farber, T. A. Vanderah, R. S. Roth, B. H. Toby, *J. Solid State Chem.* **2003**, *175*, 170.
[11] E. Sawaguchi, *J. Phys. Soc. Jpn.* **1953**, *8*, 615.
[12] A. K. Tagantsev, K. Vaideeswaran, S. B. Vakhrushev, A. V. Filimonov, R. G. Burkovsky, A. Shaganov, D. Andronikova, A. I. Rudskoy, A. Q. Baron, H. Uchiyama, D. Chernyshov, A. Bosak, Z. Ujma, K. Roleder, A. Majchrowski, J.-H. Ko, N. Setter, *Nat. Commun.* **2013**, *4*, 2229.
[13] M. E. Strayer, A. Sen Gupta, H. Akamatsu, S. Lei, N. A. Benedek, V. Gopalan, T. E. Mallouk, *Adv. Funct. Mater.* **2016**, *26*, 1930.
[14] R. Zhang, M. S. Senn, M. A. Hayward, *Chem. Mater.* **2016**, *28*, 8399.
[15] P. V. Balachandran, D. Puggioni, J. M. Rondinelli, *Inorg. Chem.* **2014**, *53*, 336.
[16] R. Zhang, A. S. Gibbs, W. Zhang, P. S. Halasyamani, M. A. Hayward, *Inorg. Chem.* **2017**, *56*, 9988.
[17] M. Retuerto, M. R. Li, I. Ignatov, M. Croft, K. V. Ramanujachary, S. Chi, J. P. Hodges, W. Dachraoui, J. Hadermann, T. T. Tran, P. S. Halasyamani, C. P. Grams, M. Greenblatt, *Inorg. Chem.* **2013**, *52*, 12482.
[18] S. N. Ruddlesden, P. Popper, *Acta Crystallogr.* **1958**, *11*, 54.
[19] N. A. Benedek, C. J. Fennie, *Phys. Rev. Lett.* **2011**, *106*, 107204.
[20] E. Bousquet, M. Daeber, N. Stucki, C. Lichtensteiger, P. Hermet, S. Gariglio, J.-M. Triscone, P. Ghosez, *Nature* **2008**, *452*, 732.
[21] M. S. Senn, A. Bombardi, C. A. Murray, C. Vecchini, A. Scherillo, X. Luo, S. W. Cheong, *Phys. Rev. Lett.* **2015**, *114*, 035701.
[22] M. J. Pitcher, P. Mandal, M. S. Dyer, J. Alaria, P. Borisov, H. Nui, J. B. Claridge, M. J. Rosseinsky, *Science* **2015**, *347*, 420.
[23] X. Q. Liu, J. W. Wu, X. X. Shi, H. J. Zhao, H. Y. Xhou, R. H. Qiu, W. Q. Zhang, X. M. Chen, *Appl. Phys. Lett.* **2015**, *106*, 202903.
[24] Y. Wang, F.-T. Huang, X. Luo, B. Gao, S. W. Cheong, *Adv. Mater.* **2017**, *29*, 1601288.
[25] Y. S. Oh, X. Luo, F.-T. Huang, Y. Wang, S. W. Cheong, *Nat. Mater.* **2015**, *14*, 407.
[26] T. Fukushima, A. Stroppa, S. Picozzi, J. M. Perez-Mato, *Phys. Chem. Chem. Phys.* **2011**, *13*, 12186.
[27] N. A. Benedek, *Inorg. Chem.* **2014**, *53*, 3769.
[28] T. Zhu, T. Cohen, A. S. Gibbs, W. Zhang, P. S. Halasyamani, M. A. Hayward, N. A. Benedek, *Chem. Mater.* **2017**, *29*, 9489.
[29] C. A. L. Dixon, J. A. McNulty, K. S. Knight, A. S. Gibbs, P. Lightfoot, *Crystals* **2017**, *7*, 135.
[30] E. E. McCabe, E. Bousquet, C. P. J. Stockdale, C. A. Deacon, T. T. Tran, P. S. Halasyamani, M. C. Stennett, N. C. Hyatt, *Chem. Mater.* **2015**, *27*, 8298.
[31] H. G. Kim, T. T. Tran, W. Choi, T.-S. You, P. S. Halasyamani, K. M. Ok, *Chem. Mater.* **2016**, *28*, 2424.
[32] X.-Z. Lu, J. M. Rondinelli, *Nat. Mater.* **2016**, *15*, 951.
[33] X.-Z. Lu, J. M. Rondinelli, *Adv. Funct. Mater.* **2017**, *27*, 1604312.
[34] V. Longo, D. Minichelli, *Ceramurgia* **1974**, *4*, 25.
[35] A. T. Mulder, N. A. Benedek, J. M. Rondinelli, C. J. Fennie, *Adv. Funct. Mater.* **2013**, *23*, 4810.
[36] L.-F. Huang, X.-Z. Lu, J. M. Rondinelli, *Phys. Rev. Lett.* **2016**, *117*, 115901.
[37] A. M. Glazer, *Acta Crystallogr., Sect. B* **1972**, *28*, 3384.
[38] S. A. Denev, T. T. A. Lummen, E. Barnes, A. Kumar, V. Gopalan, *J. Am. Ceram. Soc.* **2011**, *94*, 2699.
[39] S. K. Aleksandrov, *Crystallogr. Rep.* **1995**, *40*, 251.

[40] N. A. Benedek, A. T. Mulder, C. J. Fennie, *J. Solid State Chem.* **2012**, *195*, 11.
[41] D. Orobengoa, C. Capillas, M. I. Aroyo, J. M. Perez-Mato, *J. Appl. Crystallogr.* **2009**, *42*, 820.
[42] E. A. Nowadnich, C. J. Fennie, *Phys. Rev. B* **2016**, *94*, 104105.
[43] Z. Zhou, Q. Yang, M. Liu, Z. Zhang, X. Zhang, D. Sun, T. Nan, N. Sun, X. Chen, *Spin* **2015**, *5*, 1530001.
[44] B. Xu, J. Iniguez, L. Bellaiche, *Nat. Commun.* **2017**, *8*, 15682.
[45] H. M. Rietveld, *J. Appl. Crystallogr.* **1969**, *2*, 65.
[46] F. Izumi, K. Momma, *Solid State Phenom.* **2007**, *130*, 15.
[47] J. Rodríguez-Carvajal, *Phys. B: Condens. Matter* **1993**, *192*, 55.
[48] P. E. Blöchl, *Phys. Rev. B.* **1994**, *50*, 17953.
[49] G. Kresse, D. Joubert, *Phys. Rev. B* **1999**, *59*, 1758.
[50] J. P. Perdew, K. Burke, M. Ernzerhof, *Phys. Rev. Lett.* **1996**, *77*, 3865.
[51] J. P. Perdew, K. Burke, M. Ernzerhof, *Phys. Rev. Lett.* **1997**, *78*, 1396.
[52] J. P. Perdew, A. Ruzsinszky, G. C. Csonka, O. A. Vydrov, G. E. Scuseria, L. A. Constantin, X. Zhou, K. Burke, *Phys. Rev. Lett.* **2008**, *100*, 136406.
[53] G. Kresse, J. Hafner, *Phys. Rev. B* **1993**, *48*, 13115.
[54] G. Kresse, J. Hafner, *J. Phys. Rev. B* **1993**, *47*, 558.
[55] G. Kresse, J. Furthmüller, *Comput. Mater. Sci.* **1996**, *6*, 15.
[56] G. Kresse, J. Furthmüller, *Phys. Rev. B* **1996**, *54*, 11169.
[57] A. Togo, I. Tanaka, *Scr. Mater.* **2015**, *108*, 1.
[58] Y. Hinuma, A. Togo, H. Hayashi, I. Tanaka, http://arxiv.org/abs/1506.01455 (accessed: November 2017).
[59] W. Setyawan, S. Curtarolo, *Comput. Mater. Sci.* **2010**, *49*, 299.
[60] Y. Hinuma, G. Pizzi, Y. Kumagai, F. Oba, I. Tanaka, *Comput. Mater. Sci.* **2017**, *128*, 140.
[61] A. Togo, I. Tanaka, *Phys. Rev. B* **2013**, *87*, 184104.
[62] H. Akamatsu, K. Fujita, T. Kuge, A. S. Gupta, A. Togo, S. Lei, F. Xue, G. Stone, J. M. Rondinelli, L.-Q. Chen, I. Tanaka, V. Gopalan, K. Tanaka, *Phys. Rev. Lett.* **2014**, *112*, 187602.
[63] A. Sen Gupta, H. Akamatsu, F. G. Brown, M. A. T. Nguyen, M. E. Strayer, S. Lapidus, S. Yoshida, K. Fujita, K. Tanaka, I. Tanaka, T. E. Mallouk, V. Gopalan, *Chem. Mater.* **2017**, *29*, 656.
[64] K. Momma, F. Izumi, *J. Appl. Crystallogr.* **2011**, *44*, 1272.